Stiffness and strength of suture joints in nature

Yaning Li,[1,2] Christine Ortiz,[1] and Mary C. Boyce[2,*]

[1]*Department of Materials Science and Engineering, Massachusetts Institute of Technology, Cambridge, Massachusetts 02139, USA*

[2]*Department of Mechanical Engineering, Massachusetts Institute of Technology, Cambridge, Massachusetts 02139, USA*

(Received 17 September 2011; published 29 December 2011)

Suture joints are remarkable mechanical structures found throughout nature composed of compliant interlocking seams connecting stiffer components. This study investigates the underlying mechanisms and the role of geometry governing the unique mechanical behavior of suture joints. Analytical and numerical composite models are formulated for two suture geometries characterized by a single repeating wavelength (e.g., triangular and rectangular). Stiffness, strength, and local stress distributions are predicted to assess variations in deformation and failure mechanisms. A unique homogeneous stress field is observed throughout both the skeletal and interfacial components of the triangular geometry, thus providing advantages in load transmission, weight, stiffness, strength, energy absorption, and fatigue over the rectangular geometry. The results obtained have relevance to biomimetic design and optimization, suture growth and fusion, and evolutionary phenotype diversity.

DOI: 10.1103/PhysRevE.84.062904 PACS number(s): 87.85.G−, 62.20.de, 62.20.mm

Many natural structures have evolved and adapted to improve their functional performance by making efficient use of available resources, fabricating hierarchical material microstructures with innovative geometric designs [1–3]. Biological suture joints are one elegant example whereby two stiff skeletal components interlock together via a more compliant interfacial seam, thereby providing flexibility for accommodating growth, respiration, and/or locomotion [4–7]. This topic is one of great interest for many fields, including biophysics (e.g., cranial suture growth [8]), materials physics (e.g., hierarchical structure-property relationships [9]), mechanical design (e.g., geometric mechanisms for achieving strength, stiffness, and fatigue [10]), biomimetics (e.g., bioinspired flexible armor [11]), paleontology (e.g., understanding ammonite diversity through mass extinctions [12]), and evolutionary biology (e.g., consequences of phenotypic divergence [13]).

The wavy, mechanically interdigitating structure of a suture joint can be as simple as a sinusoid [14] or exhibit a complex multiple wavelength pattern and/or a hierarchical fractal-like structure of shorter wavelengths superposed onto longer wavelengths [15–17]. A common measure of the degree of interdigitation is the "suture complexity index" or SCI [5,18,19], given in its simplest form as the ratio of the suture contour length to the shortest suture line length [l/l_0, Fig. 1(a)]. The SCI does not capture suture geometry, as different geometries can possess the same SCI.

Suture joints have been studied experimentally [4,5] and through finite element modeling [7,20]. The mechanical properties show positive correlations with the degree of interdigitation (SCI). These intriguing results motivate questions on the underlying mechanisms and the role of the detailed geometry governing the unique mechanical behavior of suture joints. Here, this question is addressed by the formulation of a scale-independent composite, elastic micromechanical model of a periodic sawtooth suture geometry. This physical model includes geometric, compositional, and material parameters that describe the detailed structure of the suture, which are varied over a large range. The mechanical behavior and properties of two model single wavelength suture geometries (e.g., triangular and rectangular) are compared by determining load transmission pathways and predicting stiffness, strength, local stress distributions, and failure mechanisms.

A schematic of a periodic suture joint with an arbitrary sawtooth geometry is shown in Fig. 1(a) and is described by the amplitude A, the wavelength λ, and the thickness of the interfacial layer g. To describe sawtooth shape, a local coordinate system x-y is set up at the apex (tip) of one tooth as shown in Fig. 1(b). The shape profile of the tooth can be described as a function $y = f(x)$, where $f(x)$ is a single-valued analytic function.

The mechanical response of a suture joint is determined for the case of tensile loading within the suture plane and normal to the suture axis, a prevalent physiologic loading condition [4–7] [Fig. 1(a)]. Stress is transmitted to the teeth through shearing of the interfacial layer. Using the free body diagram shown in Fig. 1(b), force equilibrium yields the relationship between the normal stress within the tooth, $\sigma(x)$, and the interfacial shear and normal stress, $\tau(x)$ and $\tau_n(x)$:

$$\begin{aligned}&\tau(x)dx + \tau_n(x)f'(x)dx\\ &\quad = [\sigma(x) + d\sigma][f(x) + df] - \sigma(x)f(x),\end{aligned} \tag{1a}$$

where $\tau_n(x) = f'(x)\tau(x)$. Using the Cauchy-Schwarz inequality (e.g., Ref. [21]), we can show that a uniform stress distribution corresponds to the minimum strain energy for a certain average stress. By taking $\sigma'(x) = 0$ in Eq. (1a), we obtain

$$\tau = \frac{f'(x)}{1 + [f'(x)]^2}\sigma \quad [f'(x) \neq 0]. \tag{1b}$$

From Eq. (1b), we can see that if $f'(x)$ is constant, the stresses in both phases are uniform. Therefore, $f'(x) =$ constant is a necessary condition to achieve uniform stress. The stress distribution must also satisfy the boundary conditions. When $f'(x) = 0$ (rectangular teeth), $\sigma'(x)$ cannot be zero, otherwise, τ is zero. Furthermore, the traction boundary conditions cannot be satisfied in the rectangular and general trapezoidal [when

*mcboyce@MIT.EDU

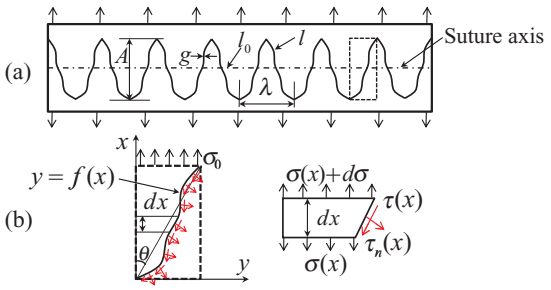

FIG. 1. (Color online) Schematic of a periodic suture joint with arbitrarily shaped teeth. (a) Geometric parameters and loading. (b) Free body diagram of an isolated tooth.

$f(0) \neq 0$] cases, if the stress were uniform (where σ must be zero at $x = 0$ and $\sigma = \sigma_0$ at $x = A$). Therefore, the solution of uniform stress in teeth is satisfied if and only if the tooth geometry is triangular. By substituting $f'(x) = \tan\theta$ [θ is defined as the tip angle of the triangular tooth, as shown in Fig. 1(b)] in Eq. (1b), we find that for a triangular suture joint, the relationship between τ and σ is simply dependent on the tooth tip angle θ:

$$\tau = \sigma \sin\theta \cos\theta. \tag{2}$$

The implications of a uniform stress in a triangular sawtooth geometry are profound, particularly regarding strength and fatigue, as will be discussed later. We will focus on analyzing this optimum triangular suture geometry for the remainder of this Brief Report. For comparison, a rectangular suture geometry (which has the closed-form solution through the well-known shear-lag model of fiber-reinforced composites [22]) is also analyzed.

Composite micromechanical models of representative volume elements (RVEs) of triangular and rectangular suture joints were constructed which represent both the skeletal components and interface adherend region [Fig. 2(a)]. The RVE of the composite structure includes a top (upper row) and bottom (lower row) row of skeletal "teeth" which interdigitate and are perfectly bonded to a thin interfacial layer (zigzag layer between the teeth). The skeletal and interfacial phases are taken to exhibit isotropic linear elastic behavior. The shape of the suture joints is described by two nondimensional parameters: the skeletal volume fraction $f_v = (\lambda - 2g)/\lambda$, and the tooth apex angle θ. The influence of geometry on the mechanical behavior of the suture joint is examined by fixing f_v and altering θ, or vice versa. The rectangular geometry is similarly described where θ [Fig. 2(a)] is related to the rectangular tooth aspect ratio through $\alpha = 2A/(\lambda - 2g) = 1/\tan\theta$. Also, the SCI i is related to θ via $i = f_v/\sin\theta$.

The result of a uniform stress in both the skeletal and interface phases is a remarkable feature of the triangular-shaped suture joint and was further supported by numerical finite element results [Figs. 2(b) and 2(c)]. Such constant stress structures imply an advantage for strength since the entire structure is equally participating in bearing the applied load and all material is fully utilized.

In the rectangular suture, stress is also transmitted to the teeth through shearing of the interfacial layer. However,

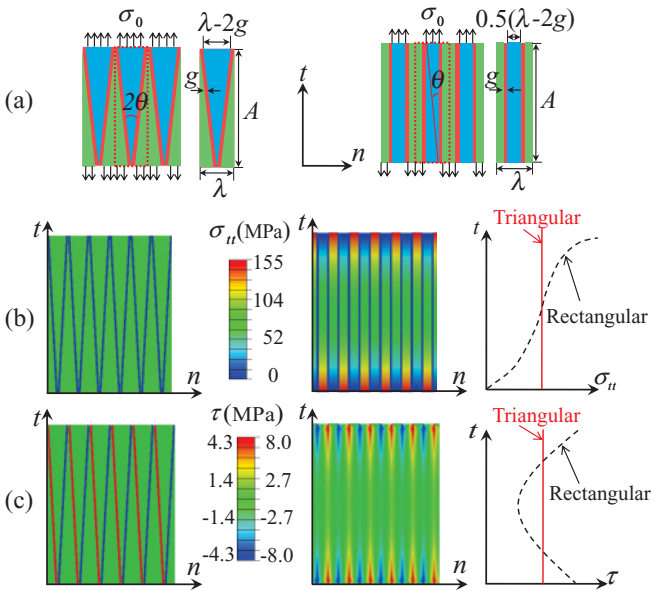

FIG. 2. (Color online) (a) Representative volume elements (RVEs) of a triangular suture (left) and a rectangular suture (right) under tension; (b) contour and line plots of the normal stress distribution in the skeletal teeth; and (c) the shear stress distribution in the interfacial layer (taken at an effective tensile strain of 1%, for a representative case of $f_v = 0.8$, $\theta = 2.9°$, skeletal Young's modulus $E_1 = 10$ GPa, and the adhesive Young's modulus $E_0 = 100$ MPa). Note that the triangular RVE and the rectangular RVE neglect bonding of the tooth tip and top edge, respectively, due to the negligible influence on suture stiffness and strength.

the interfacial shear is distributed, with higher magnitude at the tooth ends. This stress transfer is captured by the shear-lag model [22] and has also been used to study the biological composite nacre [23,24]. The shear-lag model reveals that the stress varies within the tooth, reaching a maximum value at the root of a tooth [Fig. 2(b), right].

The uniform stress distribution in the triangular suture yields a significant improvement in strength compared to the rectangular suture. At any applied strain, the maximum normal stress in the teeth and the maximum shear stress in the interface of the rectangular suture are approximately twice those in the triangular suture, as shown in Figs. 2(b) and 2(c).

To quantify the strength of the suture joints, for $2\theta < 90°$, two failure modes are assumed: tooth failure at a critical tensile stress σ_1^f and interfacial shear failure at a critical shear stress τ_0^f. The failure mode will depend on the combination of constituent strengths σ_1^f and τ_0^f, and also the suture geometry as determined by f_v and θ. For a given σ_1^f and τ_0^f, failure maps can be constructed for the triangular and rectangular geometries as a function of θ (or tooth aspect ratio) as shown in Fig. 3.

The effective tensile strengths of the triangular and rectangular suture joints are defined as σ_T^f and σ_R^f, respectively, further normalized by the product of skeletal volume fraction f_v and skeletal strength σ_1^f. Using Eq. (2) together with σ_T^f and σ_R^f, a nondimensional effective strength of the triangular

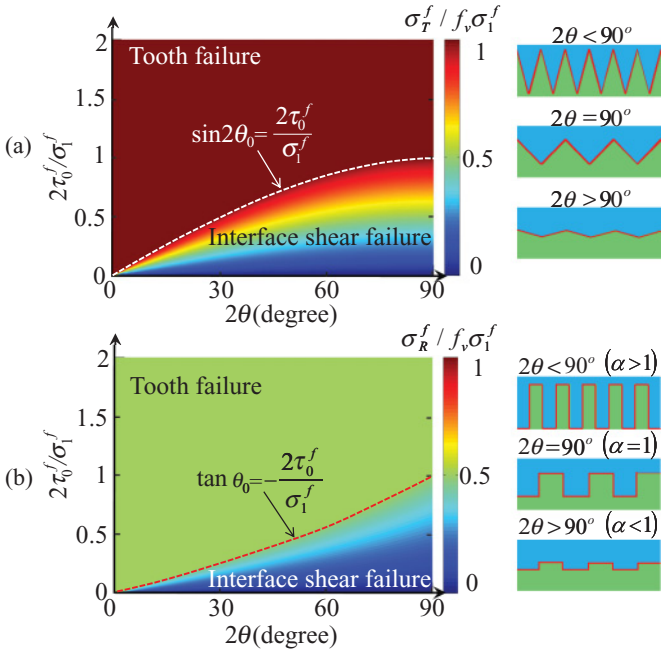

FIG. 3. (Color online) Contours of the normalized strength as a function of the component material properties and 2θ for (a) the triangular and (b) the rectangular suture joints.

suture joint is obtained:

$$\frac{\sigma_T^f}{f_v\sigma_1^f} = \min\left[1, \frac{\sin\theta_0\cos\theta_0}{\sin\theta\cos\theta}\right], \tag{3}$$

where

$$\theta_0 = \frac{1}{2}\sin^{-1}\frac{2\tau_0^f}{\sigma_1^f}, \quad \theta_0 \leqslant \frac{\pi}{4}. \tag{4}$$

θ_0 is the angle at which the skeleton and interfacial layer would simultaneously fail for a given σ_1^f and τ_0^f. For other θ, the failure mode is determined by

$$\frac{\sigma_T^f}{f_v\sigma_1^f} = \begin{cases} 1, & \theta \leqslant \theta_0 : \text{tooth failure} \\ \frac{\sin\theta_0\cos\theta_0}{\sin\theta\cos\theta}, & \theta > \theta_0 : \text{interface shear failure.} \end{cases} \tag{5}$$

For the rectangular suture joint,

$$\frac{\sigma_R^f}{f_v\sigma_1^f} = \min\left[0.5, 0.5\frac{\tan\theta_0}{\tan\theta}\right], \tag{6}$$

where

$$\theta_0 = \tan^{-1}\frac{2\tau_0^f}{\sigma_1^f}, \quad \theta_0 < \frac{\pi}{2}. \tag{7}$$

The failure mode is determined by

$$\frac{\sigma_R^f}{f_v\sigma_1^f} = \begin{cases} 0.5, & \theta \leqslant \theta_0 : \text{tooth failure} \\ 0.5\frac{\tan\theta_0}{\tan\theta}, & \theta > \theta_0 : \text{interface shear failure.} \end{cases} \tag{8}$$

Note that Eq. (3) is a precise expression for the strength of a triangular suture joint, whereas Eq. (6) gives an upper bound for the rectangular suture joint strength and corresponds to the highest interface load transmission.

Failure maps obtained using Eqs. (3) and (6) are plotted in Fig. 3 and reveal the dramatic advantage of the triangular morphology in providing strength. In Fig. 3(a), taking an example case with a strength ratio of $2\tau_0^f/\sigma_1^f = 0.3$, a triangular suture joint with $2\theta = 15^\circ$ exhibits tooth failure, giving a suture joint strength of $\sigma_T^f = f_v\sigma_1^f$, whereas for $2\theta = 60^\circ$ the suture joint will fail by interfacial shear at $\sigma_T^f = 0.35 f_v\sigma_1^f$. In comparison, in Fig. 3(b) the rectangular geometry with $2\tau_0^f/\sigma_1^f = 0.3$ exhibits the following scenarios: at $2\theta = 15^\circ$, tooth failure at $\sigma_R^f = 0.5 f_v\sigma_1^f$, and at $2\theta = 60^\circ$, interfacial shear failure at $\sigma_R^f = 0.26 f_v\sigma_1^f$. Hence, a transition in failure mode is observed from tooth failure at a high degree of interdigitation to interface shear failure at a low degree of interdigitation. The maximum strength of both suture joints is achieved in the tooth failure mode. Remarkably, the maximum strength of the triangular suture joint is twice that of the rectangular suture joint, quantitatively showing the importance of geometry in governing mechanical performance.

The micromechanical model is now extended to calculate the effective stiffness of the suture joint, $\bar{E}$. The Young's modulus of the skeletal phase is taken to be E_1 and the Young's modulus and the shear modulus of the adhesive layer to be E_0 and G_0, respectively. From the previous analysis of the stress distribution in the teeth and the interfacial layer together with a kinematic analysis of the contribution of the teeth and the interfacial layer to the imposed deformation, $\bar{E}$ of the triangular suture joint is derived as a function of the geometric and material parameters as

$$\frac{\bar{E}}{E_1}\left(f_v, \theta, \frac{E_1}{G_0}, \frac{E_1}{E_0}\right) = \frac{f_v^2}{(1-f_v)\left(\frac{E_1}{G_0}\sin^2\theta\cos^2\theta + \frac{E_1}{E_0}\sin^4\theta\right) + f_v}. \tag{9}$$

When $\theta \to 0$, $\bar{E}/E_1 \to f_v$ (i.e., approaching rule of mixtures scaling).

For the rectangular suture joint with large stiffness ratio E_1/E_0, $\bar{E}$ is derived to be

$$\frac{\bar{E}}{E_1}\left(f_v, \theta, \frac{E_1}{G_0}\right) = \frac{f_v^2}{\frac{E_1}{G_0}(1-f_v)(\tan\theta)^2 + f_v}. \tag{10}$$

Finite element models for stiffness ratios $R_s = E_1/E_0 = 10$, 100, and 1000, different f_v, and different θ are also constructed and simulation results are in complete agreement with Eq. (9) [Figs. 4(a)–4(c)]. $\bar{E}/E_1$ increases monotonically with f_v and decreases with θ as shown in Figs. 4(a) and 4(b), respectively. For large $f_v > 80\%$, the $\bar{E}/E_1$ of the triangular suture joint approaches 1 ($\bar{E}/E_1 \to 1$) and increases more rapidly with an increase in R_s. Recalling the relationships between the SCI (i) and θ, $i = f_v/\sin\theta$, the stiffness is alternately plotted as a function of i in Fig. 4(c), showing $\bar{E}/E_1$ to increase with increasing i toward the rule of mixtures scaling.

A final comparison of the stiffness and strength performance of the triangular vs. rectangular suture joint geometry is shown in the stress-strain curves of Fig. 5. Here, the case of $f_v = 0.80$ is considered with the material properties of bone and collagen $E_1 = 10$ GPa, $E_0 = 100$ MPa, $\sigma_1^f = 100$ MPa, and $\tau_0^f = 20$ MPa [23,25,26] taken as an example.

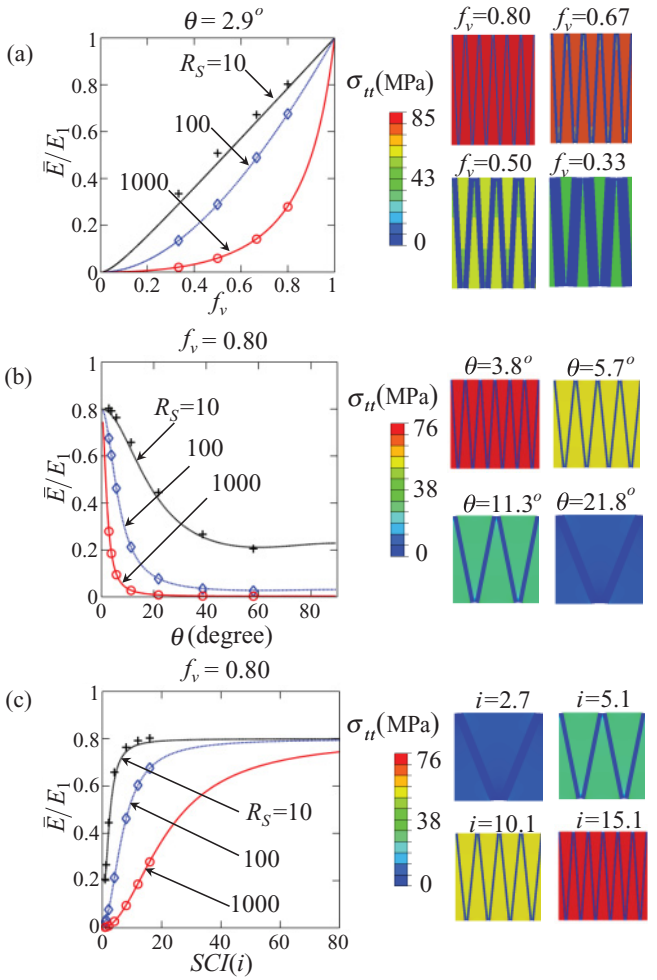

FIG. 4. (Color online) Comparison of the numerical and analytical results of the effective stiffness of the triangular suture joint [the symbols represent the finite element results; the lines represent the analytical results of Eq. (9)]: (a) influence of f_v, (b) influence of θ, and (c) influence of i.

As evident in the slope of the stress-strain curves, the stiffness increases as θ decreases. The triangular geometry provides higher stiffness compared to the rectangular case with a 20% advantage for $\theta > 20^\circ$ and the two coinciding for very small θ. The triangular suture geometry also provides higher strength for all cases. In particular, at small θ where the stiffnesses of the two geometries are nearly equivalent, the triangular suture joint exhibits twice the strength of the rectangular.

Using Eq. (4), the strength-optimized θ for the triangular suture joint is $\theta_0 = 11.8^\circ$, while for this rectangular suture, from Eq. (7), $\theta_0 = 21.8^\circ$ or aspect ratio $\alpha = 2.5$. These angles correspond to the shift of failure mode, as also shown in Fig. 5, from tooth failure to interface shear failure.

In summary, this study quantitatively explores the underlying mechanisms and the role of structure and geometry in governing the mechanical behavior of suture joints. For the triangular suture joint, a unique homogeneous stress field was observed throughout the entire composite structure (e.g., in both the skeletal and interfacial components). Hence, the triangular geometry exhibits a significant strength and stiffness advantage compared to sutures with rectangular geometry.

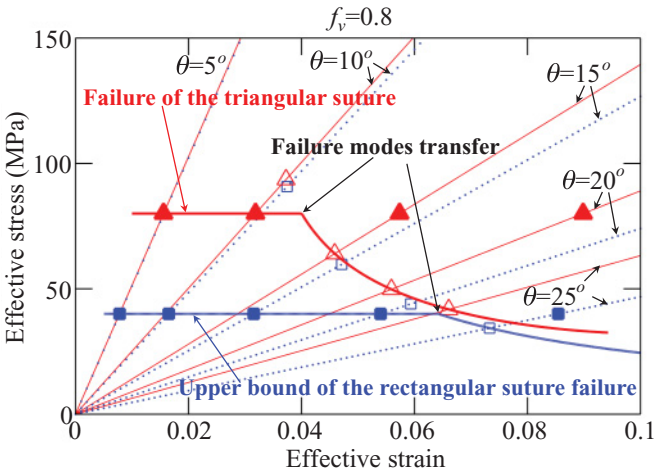

FIG. 5. (Color online) Prediction of the stiffness, strength, and failure modes of the triangular and rectangular suture joints with $f_v = 80\%$ (thin red solid lines: triangular suture; blue dotted lines: rectangular suture. "▲" and "Δ" represent the points of tooth failure and interface shear failure modes of the triangular suture joint, respectively; "■" and "□" represent those for the rectangular suture joint).

The uniform tensile stress indicates that the entire skeleton is equally bearing the applied load and, hence, the material is optimally used, providing a weight and a volume advantage to meet a given strength. The spatial homogeneity of the stress also has implications on fatigue life where suture joints often undergo cyclic tensile loading as part of their function. The transition in failure mechanism (skeletal failure to interfacial shear), as well as the stiffness and strength of the suture are found to be nonlinearly tunable by altering the suture geometric and material parameters which tailor the interface shape, degree of interdigitation, complexity, and composition. The failure maps also point to the advantage of increasing the shear strength of the interfacial layer as a means of transitioning the failure mode and achieving the upper bound in suture strength with a triangular geometry. It is clear that nature varies these geometric parameters of sutures to achieve spatial variations in mechanical properties within individual biological structures as needed for necessary functionality [27]. Such variations also exist between species and are expected to be closely related to evolutionary and phenotypic diversity [27]. This work provides a foundation for our ongoing work in assessing the role and influence of heterogeneities, spatial gradients, and hierarchically structured interfaces to further optimize mechanical performance of suture joints. The equations and design principles formulated can be employed to guide biomimetic design.

We gratefully acknowledge the support of the U.S. Army through the MIT Institute for Soldier Nanotechnologies (Contract No. DAAD-19-02-D0002), and the National Security Science and Engineering Faculty Fellowship Program (N00244-09-1-0064). Thanks also go to Juha Song at MIT for numerous helpful discussions and Dr. Carolyn R. Jaslow at Rhodes College for kindly mailing her paper reprints to us.

[1] U. G. K. Wegst and M. F. Ashby, Philos. Mag. **84**, 2167 (2004).
[2] C. Ortiz and M. C. Boyce, Science **19**, 1053 (2008).
[3] J. W. C. Dunlop and P. Fratzl, Annu. Rev. Mater. Res. **40**, 1 (2010).
[4] R. P. Hubbard, J. W. Melvin, and I. T. Barodawa, J. Biomech. **4**, 491 (1971).
[5] C. R. Jaslow, J. Biomech. **23**, 313 (1990).
[6] S. W. Herring, Front Oral Biol. **12**, 41 (2008).
[7] S. C. Jasinoski, B. D. Reddy, K. K. Louw, and A. Chinsamy, J. Biomech. **43**, 3104 (2010).
[8] S. M. Warren, L. J. Brunet, R. M. Harland, A. N. Economides, and M. T. Longaker, Nature (London) **422**, 625 (2003).
[9] S. Krauss, E. Monsonego-Ornan, E. Zelzer, P. Fratzl, and R. Shahar, Adv. Mater. **21**, 407 (2009).
[10] J. A. Motherway, P. Verschueren, G. Van der Perre, J. V. Sloten, and M. D. Gilchrist, J. Biomech. **42**, 2129 (2009).
[11] T. Arciszewski and J. Cornell, *Intelligent Computing in Engineering and Architecture*, 32 (Springer, Berlin, 2006), pp. 32–53.
[12] W. B. Saunders, D. M. Work, and S.V. Nikolaeva, Science **286**, 760 (1999).
[13] Q. Wang, L. A. Opperman, L. M. Havill, D. S. Carlson, and P. C. Dechow, Anat. Rec. Part A **288A**, 1042 (2006).
[14] J. L. Borke, G. Zhang, J. C. Yu, and C. M. Isales, J. Dent. Res. 82 (2003).
[15] T. M. Lutz and G. E. Boyajian, Paleobiology **21**, 329 (1995).
[16] J. A. Perez-Claros, P. Palmqvist, and F. Oloriz, Math. Geol. **34**, 323 (2002).
[17] W. C. Hartwig, J. Morphol. **210**, 289 (1991).
[18] W. B. Saunders and D.M. Work, Paleobiology **22**, 189 (1996).
[19] F. V. De Blasio, Lethaia **41**, 15 (2008).
[20] M. Moazen, N. Curtis, P. O'Higgins, M. E. H. Jones, S. E. Evans, and M. J. Fagan, Proc. R. Soc. London, Ser. B **276**, 39 (2009).
[21] Y. Li, A. M. Waas, and E. M. Arruda, J. Mech. Phys. Solids **59**, 43 (2011).
[22] T. H. Courtney, *Mechanical Behavior of Materials* (Waveland Press, Inc., Long Grove, 2000).
[23] B. H. Ji and H. J. Gao, J. Mech. Phys. Solids **52**, 1963 (2004).
[24] A. P. Jackson, J. F. V. Vincent, and R. M. Turner, Proc. R. Soc. London, Ser. B **234**, 415 (1988).
[25] T. L. Norman, D. Vashishth, and D. B. Burr, J. Biomech. **28**, 309 (1995).
[26] I. Jager and P. Fratzl, Biophys. J. **79**, 1737 (2000).
[27] J. H. Song, S. Reichert, I. Kallai, D. Gazit, M. Wund, M. C. Boyce, and C. Ortiz, J. Struct. Biol. **171**, 318 (2010).